

Alkali-Rich Antiperovskite  $M_3FCh$  ( $M = Li, Na$ ;  $Ch = S, Se, Te$ ): The Role of Anions in Phase Stability and Ionic TransportSusumu Fujii,<sup>#</sup> Shenghan Gao,<sup>#</sup> Cédric Tassel, Tong Zhu, Thibault Broux, Koji Okada, Yuto Miyahara, Akihide Kuwabara,<sup>\*</sup> and Hiroshi Kageyama<sup>\*</sup>Cite This: <https://doi.org/10.1021/jacs.1c04260>

Read Online

ACCESS |



Metrics &amp; More

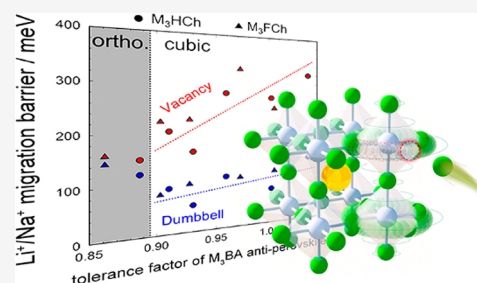


Article Recommendations



Supporting Information

**ABSTRACT:** To improve ionic conductivity, solid-state electrolytes with polarizable anions that weakly interact with mobile ions have received much attention, a recent example being lithium/sodium-rich antiperovskite  $M_3HCh$  ( $M = Li, Na$ ;  $Ch = S, Se, Te$ ). Herein, in order to clarify the role of anions in antiperovskites, the  $M_3FCh$  family, in which the polarizable  $H^-$  anion at the octahedral center is replaced by the ionic  $F^-$  anion, is investigated theoretically and experimentally. We unexpectedly found that the stronger attractive interaction between  $F^-$  and  $M^+$  ions does not slow down the  $M^+$  ion diffusion, with the calculated energy barrier being as low as that of  $M_3HCh$ . This fact suggests that the low-frequency rotational phonon modes of the octahedron of cubic  $M_3FCh$  (and  $M_3HCh$ ) are intrinsic to facilitate the fast ionic diffusion. A systematic analysis further reveals a correlation between the tolerance factor  $t$  and the ionic transport: as  $t$  decreases within the cubic phase, the rotational mode becomes softer, resulting in the reduction of the migration energy. The cubic iodine-doped  $Li_3FSe$  has a room-temperature ionic conductivity of  $5 \times 10^{-5}$  S/cm with a bulk activation energy of 0.18 eV.



## 1. INTRODUCTION

Perovskite oxides  $ABO_3$  have attracted tremendous research interests for decades owing to their diverse functionalities.<sup>1–5</sup> They ideally adopt cubic structures, but in many cases,  $BO_6$  octahedral rotation occurs to form phases with lower symmetry, driven by particular phonon modes. The structural distortion and stability of perovskites are commonly described by the Goldschmidt tolerance factor  $t$ , which indicates the size mismatch between the A- and B-site ions.<sup>6</sup> In perovskite and its layered analogues, the tolerance factor has been widely used to predict and control various physical properties, e.g., giant magnetoresistance of  $La_{0.69}Ca_{0.31}MnO_3$ ,<sup>6</sup> Mott transition of  $RNiO_3$  ( $R =$  rare earth),<sup>7</sup> oxide ion mobility in  $Ln_2NiO_{4+\delta}$  ( $Ln = La, Pr, Nd$ ),<sup>8</sup> and superconductivity of  $Ba_{1-x}K_xBiO_3$ .<sup>9,10</sup> On the other hand, the correlations between tolerance factor and structural distortions or functional properties were rarely explored in the antiperovskite (AP), the electronically inverted perovskite derivative.<sup>11</sup> Nevertheless, the cation richness and mixed anion features provide antiperovskites a diverse array of novel physical and chemical properties<sup>12–17</sup> such as topological odd-parity superconductivity in  $Sr_{3-x}SnO^{13}$  and the high  $Li^+$  ionic conductivity in  $Li_3O(Cl_{1-x}Br_x)$ .<sup>18–20</sup>

Very recently, we have synthesized a series of alkali-rich APs  $M_3HCh$  at pressures below 5 GPa ( $M = Li, Na$ ;  $Ch = S, Se, Te$ ).<sup>21</sup> Composed of a large polarizable hydride and a chalcogenide, the  $M_3HCh$  AP exhibits a low calculated migration barrier for cation hopping from one stable site to another site. The soft anionic sublattice is also found in other

superionic solid-state electrolytes such as  $Li_{10}GeP_2S_{12}$ <sup>22</sup> and  $Li_6PS_5X$  ( $X = Cl, Br, I$ ).<sup>23</sup> Another important structural characteristic in the cubic AP is the body-centered-cubic-like anion framework, which has been suggested as a rare and desirable feature for achieving high ionic conductivity.<sup>24</sup> In addition, a low-frequency phonon mode associated with the rotation of  $HM_6$  octahedra has been acknowledged as promoting fast  $Li^+/Na^+$  ion diffusion.<sup>21</sup>

From the structural perspective, the ideal cubic structure (Figure 1a) is unconventionally stable over a wide range of  $t$ ; only when  $t \leq 0.85$  does the orthorhombic  $Na_3HS$  undergo octahedral distortions (Figure 1b). The size-flexibility of hydride ions at the B-site, as seen in some oxyhydrides,<sup>25–27</sup> is attributed as stabilizing the cubic phase, but at the same time the chalcogen anions at the A-site are polarizable. In addition, although the soft rotational phonon mode has been identified, the general link between the lattice dynamics and ionic transport has not been quantified. More generally, the effect of antiperovskite cuboctahedral A- and octahedral B-sites on the mobile cations should be different, but the role of each anion remains unclear.

Received: April 25, 2021



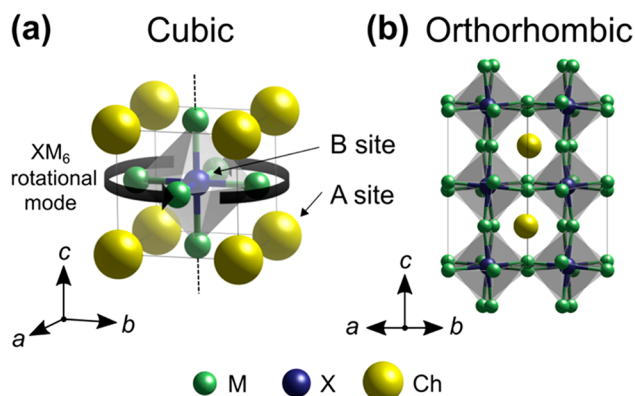


**Figure 1.** (a) Cubic  $M_3XCh$  antiperovskite (space group  $Pm\bar{3}m$ ) and (b) orthorhombic anti- $GdFeO_3$  structure (space group  $Pbnm$ ), where  $M = Li, Na$ ,  $X = F, H$ , and  $Ch = S, Se, Te$ . The low-energy phonon mode associated with the  $XM_6$  octahedral rotation is depicted in (a) using arrows.

To address these questions, we investigate a new series of APs,  $M_3FCh$ , with an ionic fluorine anion at the B-site and a polarizable chalcogen anion at the A-site. Combined with the lattice-dynamics calculations, the experimental data show that the  $M_3FCh$  ( $Ch = Se, Te$ ) adopts a cubic structure, except for orthorhombic  $Na_3FS$ . Interestingly, the much stronger M–F bond strength than that of M–H does not increase the cationic migration barrier, indicating a dominant role of the Ch anion in flattening the energy potential for the  $M^+$  jump. A systematic comparison of hydride- and fluoride-based systems further reveals a relationship between the tolerance factor, the soft rotational phonon mode, and the migration barrier: the cubic antiperovskites with low  $t$  show a low frequency of the rotational mode and thereby a low migration barrier. Furthermore, the fast Li ionic conductivity is experimentally demonstrated in the cubic iodine-doped  $Li_3FSe$ , which exhibits a conductivity of  $5 \times 10^{-5}$  S/cm at room temperature and a low bulk activation energy of 0.18 eV.

## 2. COMPUTATIONAL AND EXPERIMENTAL METHODS

**Structure Optimization.** Structure optimization of  $M_3XCh$  compounds ( $M = Li, Na$ ;  $X = H, F$ ;  $Ch = O, S, Se, Te$ ) under 0, 5, 10, and 20 GPa was performed using the plane-wave basis projector augmented wave (PAW) method<sup>28</sup> and the generalized gradient approximation (GGA) in the form of PBEsol<sup>29</sup> as implemented in the Vienna *Ab initio* Simulation Package (VASP).<sup>30,31</sup> A plane-wave energy cutoff and the criterion of total energy convergence were set to 650 eV and  $1.0 \times 10^{-6}$  eV/atom, respectively. Atomic positions and lattice constants were relaxed until the residual forces were less than  $1.0 \times 10^{-3}$  eV/Å. The Brillouin zones were sampled with  $\Gamma$ -centered  $k$ -point grids with a spacing of  $0.2 \text{ \AA}^{-1}$ . Finer  $k$ -point grids with a spacing of  $0.1 \text{ \AA}^{-1}$  were used for electronic density of states (DOS). The PAW potentials employed in this study have the following valence configurations:  $[1s^2 2s^1]$  for Li,  $[2p^6 3s^1]$  for Na,  $[1s^1]$  for H,  $[2s^2 2p^5]$  for F,  $[2s^2 2p^4]$  for O,  $[3s^2 3p^4]$  for S,  $[4s^2 4p^4]$  for Se, and  $[5s^2 5p^4]$  for Te. The rest were considered as fixed core electrons.

**Phonon Calculation.** Phonon band structures were calculated using the finite displacement method<sup>32</sup> as implemented in Phonopy.<sup>33</sup> Second-order force constants were estimated by displacing atoms with a distance of 0.01 Å from their stationary positions. Only symmetrically nonequivalent displacements were considered here. A set of supercells with  $2 \times 2 \times 2$  dimension was employed for all cubic compounds, since in  $Li_3HS$   $2 \times 2 \times 2$ ,  $3 \times 3 \times 3$ , and  $4 \times 4 \times 4$  supercells produced almost the same phonon properties.<sup>21</sup> Non-

analytical term correction<sup>34</sup> to consider the polarization was adopted, with Born effective charge tensors and dielectric constants calculated by density functional perturbation theory as implemented in VASP.<sup>30,31</sup>

We paid special attention to a specific phonon mode at the M point in cubic  $M_3XCh$  (indicated as yellow circles in Figure 2a and b)

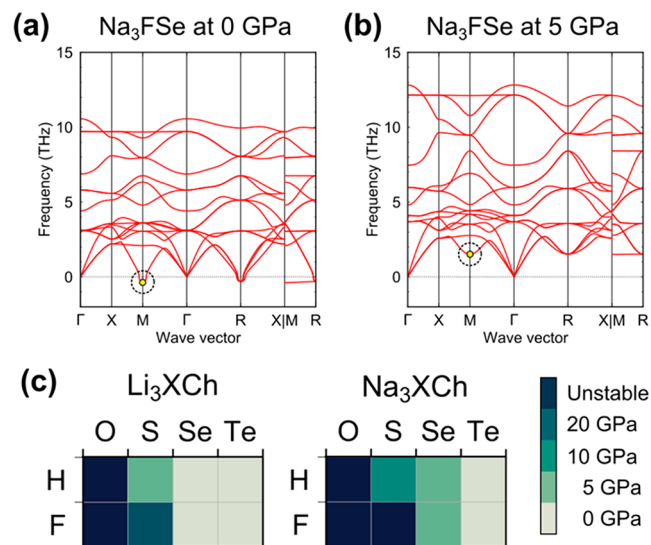


**Figure 2.** (a, b) Phonon band structures of  $Na_3FSe$  at (a) 0 and (b) 5 GPa. The negative number of the vertical axis represents imaginary frequency. (c) Calculated lowest pressure at which  $M_3XCh$  becomes dynamically stable in cubic form. Here, “unstable” refers to a compound that is not dynamically stable even at 20 GPa.

corresponding to the rotational motion of  $XM_6$  octahedra, since this mode is related to the phase transition from cubic to lower-symmetry structures and also to cationic migration pathways.<sup>21</sup> The force constant  $k_{rot}$  associated with this phonon mode under ambient pressure was estimated by the equation of simple harmonic motion,  $\omega_{rot} = \sqrt{k_{rot}/m_M}$ , where  $\omega_{rot}$  is the phonon frequency of the rotational mode and  $m_M$  is the atomic mass of M.<sup>21</sup>

**Migration Energy Barrier.** The energy barriers for cation migration via vacancy and interstitial defects were calculated using the nudged elastic band (NEB) method.<sup>35</sup> The charged supercells with the dimensions of  $3 \times 3 \times 3$  or  $2 \times 2 \times 2$  were used for cubic  $M_3FCh$  and orthorhombic  $Na_3FS$ , respectively, with the Brillouin zone sampling at one  $k$ -point (0.25 0.25 0.25). For NEB calculations, the convergence criteria for total energy and structure optimization were set to  $1.0 \times 10^{-6}$  eV/supercell and  $2.0 \times 10^{-2}$  eV/Å, respectively. The climbing image NEB method<sup>36</sup> was employed for the migration via interstitials in  $Li_3FSe$  since it exhibited two energy peaks along its migration path. The total energies of the vacancy and interstitial models calculated with the same condition were used to evaluate the formation energies of Schottky and Frenkel defects (Table S9).

**Tolerance Factor.** The stability of perovskites is generally discussed on the basis of the Goldschmidt tolerance factor  $t$ , defined as

$$t = \frac{r_A + r_M}{\sqrt{2}(r_B + r_M)}$$

where  $r_A$  and  $r_B$  are the radii of anions occupying the A- and B-sites, respectively, and  $r_M$  is the radius of M cations.<sup>37</sup> The revised effective Shannon ionic radii<sup>38</sup> were used, except for the hydride anion. Note that Ch and X ionic radii for the coordination number (CN) of six were used, although the A-site is 12-fold coordinated. This gives reasonable results as reported in previous works.<sup>20,39</sup> For the hydride anion, which can adapt to its local environment and is highly flexible

in size, we used a fixed ionic radius of 1.26 Å, the average of  $H^-$  radii in  $M_3HCh$  (determined from experimental lattice constants in our previous work<sup>21</sup>).

**Materials Synthesis.** All ternary antiperovskites were synthesized as follows:  $NaF + Na_2Ch \rightarrow Na_3FCh$  or  $LiF + Li_2Ch \rightarrow Li_3FCh$ , using as-purchased NaF (Sigma-Aldrich, 99.99%),  $Na_2S$  (Sigma-Aldrich, 99%),  $Na_2Se$  (Kojundo, 99%),  $Na_2Te$  (Kojundo, 99%), LiF (Sigma-Aldrich, 99.99%), and  $Li_2S$  (Sigma-Aldrich, 99%). The  $Li_2Se$  and  $Li_2Te$  were prepared by using  $LiEt_3BH$  (Sigma-Aldrich), Se (Rare Metallic Co., Ltd., 99.9%), and Te (Rare Metallic Co., Ltd., 99.9%) according to ref 40. The binary starting materials were mixed in an agate mortar and subsequently pressed into pellets. Typically, a pellet was inserted into a boron nitride (BN) sleeve and sealed with BN caps. Next, the sample and sleeves were inserted into a graphite tube, then enclosed in the pyrophyllite cube for high-pressure reaction. All above preparations and sample handling were done in an  $N_2$ -filled glovebox with  $O_2$  and  $H_2O$  levels below 1 ppm. The pyrophyllite cubes containing the pellets were pressed at 5 GPa and heated to 1000 °C for 1 h.

**Synchrotron X-ray Diffraction.** Powdered  $Na_3FCh$  sealed in a borosilicate capillary was investigated at the BL02B2 beamline at the SPring-8 in Japan. The software JANA2006<sup>41</sup> was used to refine the synchrotron X-ray diffraction (SXRD) data. VESTA was used to plot the crystal structures.<sup>42</sup> The Coulombic energies of the refined  $Na_3FS$  and  $Na_3HS$ <sup>21</sup> were calculated using the Generally Utility Lattice Program (GULP) code.<sup>43</sup>

**Impedance Spectroscopy.** Ionic conductivities of cold-pressed pellets of  $Na_3FCh$  were measured by electrochemical impedance spectroscopy (EIS) with a constant voltage of 100 mV in the frequency range of 1 MHz to 0.1 Hz using an SI1287 potentiostat/galvanostat with an SI1260 impedance analyzer. The powder was placed into a custom-made Swagelok cell and pressed into a 10 mm diameter between two stainless steel rods. All the sample handling and electrochemical measurements were conducted in an Ar-protected atmosphere. The EIS measurement for each composition was collected at 25, 40, 80, and 100 °C after being held for 1 h to ensure the temperature stabilization. The analysis of Nyquist plots was performed using the EC-lab software package Z-fit.

### 3. RESULTS AND DISCUSSION

**Phase Stability.** To investigate the phase stability of ideal cubic structures under pressure, we performed lattice dynamics calculations for  $M_3FCh$  ( $M = Li, Na$ ;  $Ch = O, S, Se, Te$ ) at 0, 5, 10, and 20 GPa. For comparison, we performed the same calculations for  $M_3HCh$ , which was previously studied at up to 5 GPa.<sup>21</sup> As a typical example, the phonon band structures of  $Na_3FSe$  at 0 and 5 GPa are shown in Figure 2a and b. At ambient pressure, phonon modes at the M and R points exhibit imaginary frequencies, where the former mode corresponds to the rotation of  $XM_6$  octahedra (Figure 1a), leading to lower-symmetry structures. However, the application of external pressure of 5 GPa stabilizes the cubic structure, as these imaginary frequencies disappear (Figure 2b). Similar results have been previously obtained for  $NaHSe$ .<sup>21</sup>

Figure 2c summarizes the lowest pressure where the ideal cubic AP structure gets dynamically stable. We use the term “dynamically stable” here because there may be other more “energetically stable” phases (e.g., decomposition into MF and  $M_2Ch$  binaries). With smaller chalcogenides incorporated at the A-site, a higher pressure is needed to stabilize the cubic phase for both fluoride- and hydride-based systems. Higher pressure is required to stabilize  $M_3FCh$ , compared to their hydride analogues. For example, imaginary phonon modes for  $Li_3FS$  disappear at 20 GPa, which is higher than the pressure of 5 GPa to stabilize the cubic  $Li_3HS$ . These tendencies can be understood in terms of the high compressibility of  $H^-$ , as

revealed in  $LnHO$  ( $Ln = \text{lanthanide}$ )<sup>25,26</sup> and  $SrVO_2H$ .<sup>27</sup> In fact, the computed volumes of  $H^-$  decrease more than those of  $F^-$  and  $Ch^{2-}$  ions with increasing pressure (Figure S1, Tables S1 and S2). Note that Kim et al.<sup>39</sup> showed that  $M_3FS$  and  $M_3FSe$  are energetically (not dynamically) unstable based on the decomposition energies using *ab initio* calculations at ambient pressure.

**Material Synthesis.** The above computational results motivated us to synthesize  $M_3FCh$  using a method similar to their hydride analogues.<sup>21</sup> Heating mixtures of  $M_2Ch$  and MF up to 1000 °C under 5 GPa produced  $M_3FCh$  APs, except for  $Li_3FS$  (Figure S2). No trace of  $Li_3FS$  was found under 5 GPa, in agreement with the computational results predicting that 20 GPa is required to stabilize cubic  $Li_3FS$ . The refinement of synchrotron X-ray diffraction data of  $Li_3FSe$ ,  $Li_3FTe$ ,  $Na_3FSe$ , and  $Na_3FTe$  (Figures S3–S6 and Tables S3–S5) reveals that all phases adopt the  $Pm\bar{3}m$  structure, isostructural to their hydride counterparts,<sup>21</sup> along with the small amounts of unreacted precursors. The successful synthesis of cubic  $Li_3FTe$  and  $Na_3FTe$  is reasonable given their tolerance factors  $t$  of 1.01 and 0.97. Although two other compounds,  $Li_3FSe$  and  $Na_3FSe$ , have lower  $t$  values (0.93 and 0.90), the undistorted structure is as robust as  $M_3HCh$ . This is probably due to the soft nature of A-site  $Ch^{2-}$  ions (see Figure S7 and Table S6 for the lattice parameters). The presence of imaginary phonon modes in the ambient-pressure calculation for  $Na_3FSe$  (Figure 2a) implies that the cubic phase synthesized at high pressure may be transformed into lower symmetry structures after pressure release. However, such symmetry lowering is absent in the sample quenched from 5 GPa. Similar behavior has been observed in hydride-based APs ( $Li_3HS$  and  $Na_3HSe$ ).<sup>21</sup> These observations suggest that the anharmonic effect of vibrations at finite temperature, not included in the present calculations, is responsible for the stabilization of the cubic structure, as found in  $SrTiO_3$ .<sup>44</sup>

Although cubic  $Na_3FS$  is dynamically unstable even at 20 GPa, its synchrotron X-ray diffraction pattern (Figure S8 and Table S7) shows the formation of AP together with superstructure peaks fitted to the anti-GdFeO<sub>3</sub> ( $Pbnm$ ) structure (Figure 1b). This structural distortion can be verified from its smaller  $t$  of 0.86. Given the contrasting nature of the  $F^-$  and  $H^-$  anions, the isostructural  $Na_3FS$  and  $Na_3HS$  provide an opportunity to address the question of how these anions behave in the AP structure. A close inspection of the refined structures reveals that  $FNa_6$  octahedra are less tilted than  $HNa_6$ , with averaged  $X-Na-X$  angles of 160.9° and 147.5°, respectively (Figure 3). The octahedral shape itself is also less

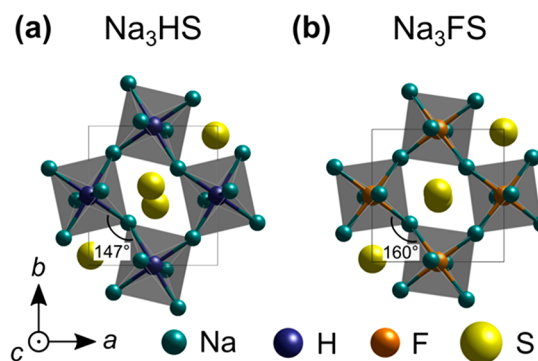
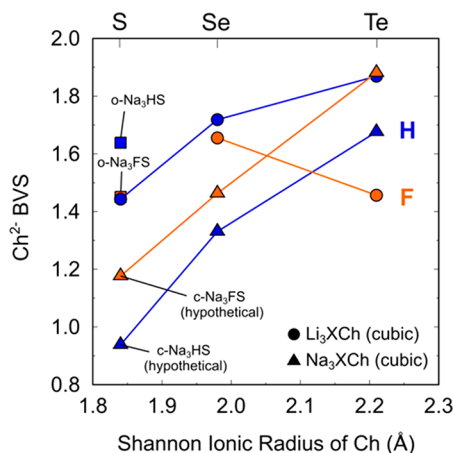


Figure 3. Refined  $Pbnm$  structure of (a)  $Na_3FS$  and (b)  $Na_3HS$ .



distorted: the  $\text{HNa}_6$  octahedron is stretched ( $2.374 \pm 0.048$  Å), whereas the  $\text{FNa}_6$  octahedron is closer to the regular octahedron with similar Na–F bond lengths ( $2.251 \pm 0.007$  Å) (Table S8). The octahedral distortion in  $\text{Na}_3\text{HS}$  is large, although not as large as those of the Jahn–Teller active  $\text{Mn}^{3+}$  and  $\text{Cu}^{2+}$  (e.g.,  $\text{Mn–O} = 2.018 \pm 0.117$  Å in  $\text{LaMnO}_3$ ).<sup>45</sup> The more ionic (covalent) nature of  $\text{F}^-$  ( $\text{H}^-$ ) is possibly responsible for these differences. When formal charges of  $(\text{M}^+)_3(\text{B}^-)(\text{A}^{2-})$  are assumed, the Coulombic energy of the refined “ $\text{Na}_3\text{FS}$ ” structure is 0.19 eV/f.u. lower than that of the refined “ $\text{Na}_3\text{HS}$ ” structure.

**Chemical Bonding.** To investigate the cubic stability of  $\text{M}_3\text{FCh}$  from the experimental perspective, the bond valence sum (BVS) values of Ch ions were estimated using the refined structures and tabulated parameters<sup>46</sup> (Figure 4). Similar to



**Figure 4.** Bond valence sum (BVS) values for  $\text{Ch}^{2-}$  ions in  $\text{M}_3\text{HCh}$ <sup>23</sup> (blue) and  $\text{M}_3\text{FCh}$  (orange).

$\text{M}_3\text{HCh}$ , the Ch ions in  $\text{M}_3\text{FCh}$  are significantly underbonded with a decrease in their ionic radius (except for  $\text{Li}_3\text{FTe}$ ), consistent with the predicted dynamic stability (Figure 2c). The BVS value of  $\text{S}^{2-}$  in  $\text{Na}_3\text{FS}$  is too low (1.18) in the hypothetical cubic form but increases to 1.45 in the orthorhombic form. This means that the octahedra tilting occurs to maximize the oxidation state of the Ch ion at the A-site, thereby stabilizing the corner-sharing framework with a lowered symmetry as in the case of  $\text{Na}_3\text{HS}$ .

As shown in Figure S9, the tolerance factors of these antiperovskites calculated on the basis of Shannon ionic radii at ambient pressure correlate well with the calculated pressure at which the cubic structure achieves dynamic stability and predict well compounds that are synthesized under high pressure. Although the soft chalcogenide anion was likely considered to exhibit a degree of compressibility under pressure, the tolerance factors are still valid for predicting the phase stability of the series of antiperovskites. We argue that a modified tolerance factor taking into account the pressure dependence of the ionic radius would be more desirable for the direct comparison with the conventional oxide perovskites.

Next, the chemical bonding in  $\text{M}_3\text{HCh}$  and  $\text{M}_3\text{FCh}$  was theoretically evaluated using the integrated crystal orbital Hamilton population (ICOHP) analysis.<sup>47–49</sup> We found that the M–F bond in  $\text{M}_3\text{FCh}$  is much stronger than the M–H bond in  $\text{M}_3\text{HCh}$  (Figures S10 and S11). Related to this, the  $\text{F}^-$  ion in the  $\text{FM}_6$  octahedral center has a nearly constant

Mulliken charge independent of chalcogen type, while the Mulliken charge for the  $\text{H}^-$  ion is variable (Figure S12). Thus, the  $\text{F}^-$  ion is more ionic compared to the  $\text{H}^-$  ion, having a covalent interaction with surrounding cations.

**Ionic Transport.** We initially expected that a strong M–F bonding (vs M–H bonding) could give a negative impact on M-ion conduction, as weaker bonding interactions between the mobile cations and polarizable anions could flatten the energy landscape for ion hopping.<sup>9,52–54</sup> However, it is unexpectedly found that the large difference in bond strength between  $\text{M}_3\text{FCh}$  and  $\text{M}_3\text{HCh}$  has little influence on the migration energy barriers  $E_a$  calculated for either the vacancy or (interstitial) dumbbell mechanism. For  $\text{M}_3\text{FCh}$ , low calculated energy barriers are achieved, 0.16–0.33 eV for the vacancy mechanism (Figure 5a) and 0.08–0.14 eV for the dumbbell

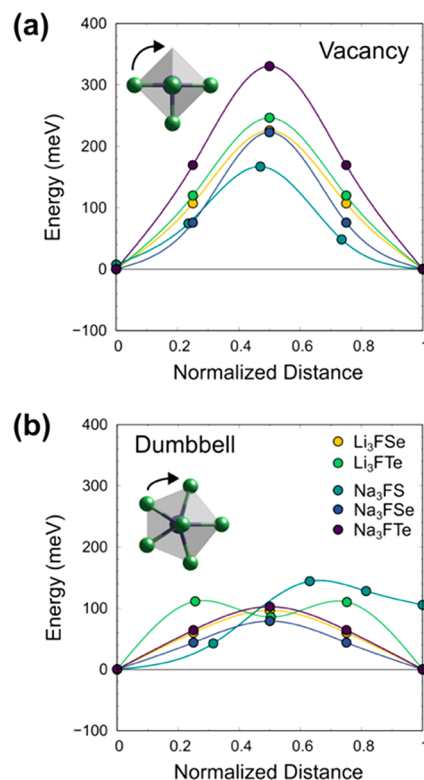


**Figure 5.** Minimum-energy migration pathways for (a) vacancy and (b) interstitial (dumbbell) mechanisms in cubic  $\text{Li}_3\text{FSe}$ ,  $\text{Li}_3\text{FTe}$ ,  $\text{Na}_3\text{FSe}$ , and  $\text{Na}_3\text{FTe}$  and orthorhombic  $\text{Na}_3\text{FS}$ . For  $\text{Na}_3\text{FS}$ , a representative migration pathway is shown because there are multiple pathways with lower-symmetry structure (see Figure S13 for details). The insets show the schematics of migration pathways around an  $\text{XM}_6$  octahedron.

mechanism (Figure 5b). These  $E_a$  values are comparable to those of  $\text{M}_3\text{HCh}$  (0.15–0.32 and 0.05–0.14 eV).<sup>21</sup> This result indicates that the A-site chalcogen anions, rather than the B-site anions, play the predominant role in fast cation transport of the APs. In other words, the soft nature of the  $\text{Ch}^{2-}$  anion in the cubic lattice mainly weakens the electrostatic interaction of  $\text{Li}^+/\text{Na}^+$  ions throughout the migration path.

Our previous study of cubic  $\text{M}_3\text{HCh}$  suggests that the fast ionic conduction is assisted by a low-energy (soft) rotational phonon mode of  $\text{HM}_6$  octahedra (Figure 1a).<sup>21</sup> For conventional ionic conductors, the lattice softness is often quantitatively correlated with the phonon frequency of the

migrating ion.<sup>50–52</sup> Here we only consider the  $\text{XM}_6$  rotational phonon mode because this mode coincides with the direction of cation migration and likely promotes cationic migration. Its phonon frequency was converted into the more intuitive force constant  $k_{\text{rot}}$  which represents the repulsion from the surrounding atoms associated with the rotational motion (see Methods for details). Figure 6 shows that the  $k_{\text{rot}}$  values

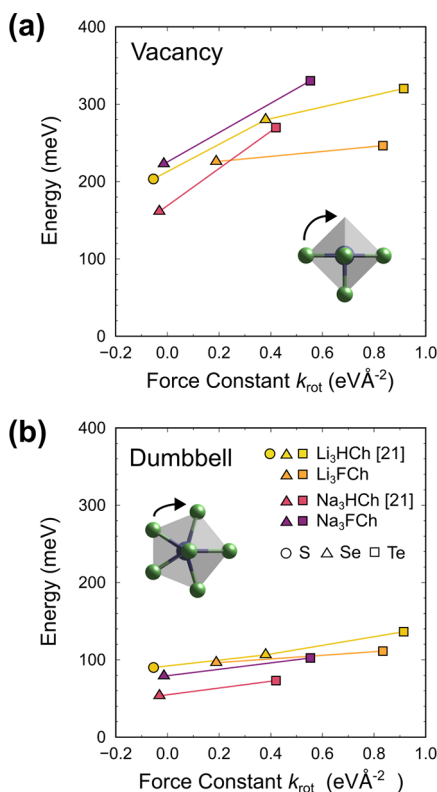


**Figure 6.** Migration energy barriers of cubic  $\text{M}_3\text{XCh}$  ( $\text{M} = \text{Li}/\text{Na}$ ;  $\text{X} = \text{H}/\text{F}$ ;  $\text{Ch} = \text{S}/\text{Se}/\text{Te}$ ) as a function of force constant  $k_{\text{rot}}$  for (a) vacancy and (b) interstitial dumbbell mechanisms.  $k_{\text{rot}}$  is associated with the  $\text{XM}_6$  rotational phonon mode at the M point (Figures 1a and 2a,b).

for  $\text{M}_3\text{FCh}$  are as low as the ones for  $\text{M}_3\text{HCh}$  and well correlate with the migration energy barrier: the smaller the force constant, the lower the energy barrier.

This correlation can be further extended to the tolerance factor  $t$ : Figure 7a clearly shows the tendency for cubic APs with smaller  $t$  to adopt smaller  $k_{\text{rot}}$ , which means that the rotational mode of  $\text{XM}_6$  becomes softened as the size mismatch increases. In other words, as  $t$  decreases, instead of readily undergoing a structural transition as in conventional perovskites, AP maintains its cubic structure and the migration energy barrier decreases (Figure 7b). Since these phonons are frozen in orthorhombic  $\text{Na}_3\text{FS}$  and  $\text{Na}_3\text{HS}$ , cubic materials near the phase boundary are considered to be the most suitable for fast ion conduction. The effect of the phase transition can be seen in the dumbbell mechanism, but not clearly in the vacancy mechanism (Figure 7b). Interestingly, the calculations of  $\text{Li}_3\text{OCl}$  and its derivatives ( $\text{M}_3\text{B}^{2-}\text{A}^-$ ) by Kim et al. show that the migration energy barrier decreases when the octahedron rotates,<sup>39</sup> which implies that swapping the valence of the A- and B-sites may change some factors influencing ion transport.

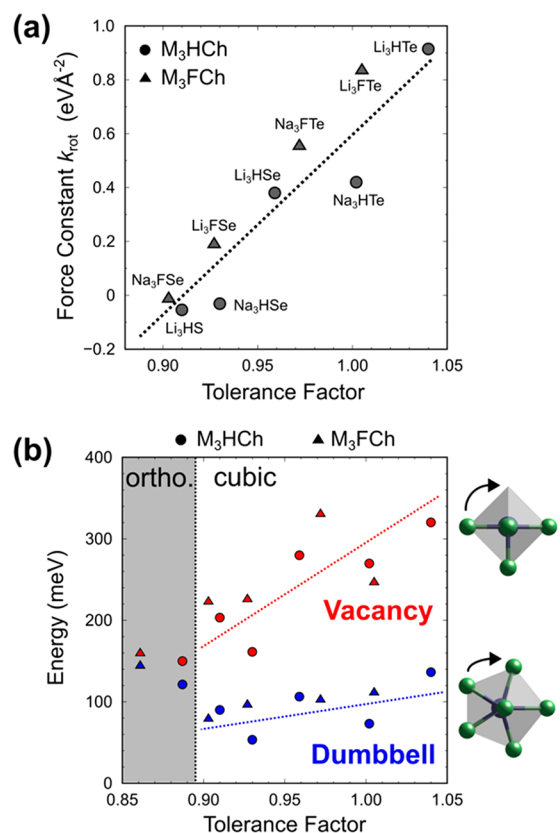


**Figure 7.** (a) Force constant  $k_{\text{rot}}$  associated with the  $\text{XM}_6$  rotational phonon mode in cubic  $\text{M}_3\text{XCh}$  ( $\text{M} = \text{Li}, \text{Na}$ ;  $\text{X} = \text{H}, \text{F}$ ;  $\text{Ch} = \text{S}, \text{Se}, \text{Te}$ ) as a function of tolerance factor. The dotted line aids in clear observation. (b) Migration energy barriers of  $\text{M}_3\text{XCh}$  as a function of tolerance factor for both vacancy and dumbbell mechanisms. The insets show the schematics of migration pathways around an  $\text{XM}_6$  octahedron.

The migration energy barriers via the dumbbell mechanism are significantly low, but the formation energies of interstitials are higher than vacancies (Table S9). Thus, a common strategy by substituting divalent chalcogenide (e.g.,  $\text{Se}^{2-}$ ) with monovalent halide (e.g.,  $\text{I}^-$ ) to create vacancy charge carriers has been tested in the cubic  $\text{Li}_3\text{FSe}$  antiperovskite.<sup>53–55</sup> A stoichiometric amount of  $\text{LiI}$  was added, and the nominal composition of  $\text{Li}_{2.9}\text{FSe}_{0.9}\text{I}_{0.1}$  was synthesized under the same condition with the pristine one. Rietveld refinement of the synchrotron X-ray diffraction data of this Li-deficient sample (Figure S14 and Table S10) suggested that the iodine successfully substituted selenium without changing the cubic symmetry and converged to the refined composition of  $\text{Li}_{2.942}\text{F}_{1.001}\text{Se}_{0.942}\text{I}_{0.058}$ . As shown in Figures 8a and S15, the Nyquist plots of the iodine-doped  $\text{Li}_3\text{FSe}$  exhibit the typical two slightly depressed semicircles at high and mid frequencies, which correspond to the bulk and grain boundary resistance, respectively, and clear polarization spike at low frequency.<sup>21,53</sup> The impedance spectra were fit to an equivalent circuit consisting of two parallel arrangements of CPE (constant phase element,  $Q$ ) and resistor ( $R$ ) in series with a CPE representing the blocking electrodes. After the introduction of a small amount of Li vacancies, the sample exhibits a high bulk  $\text{Li}^+$  conductivity of  $5 \times 10^{-5} \text{ S/cm}$  at room temperature and total conductivity of  $2 \times 10^{-4} \text{ S/cm}$  at  $100^\circ\text{C}$  (Figure 8b). Notably, the extracted bulk activation energy for Li ionic motion ( $E_{\text{a, bulk}}$ ) was as low as 0.18 eV, close to the theoretical

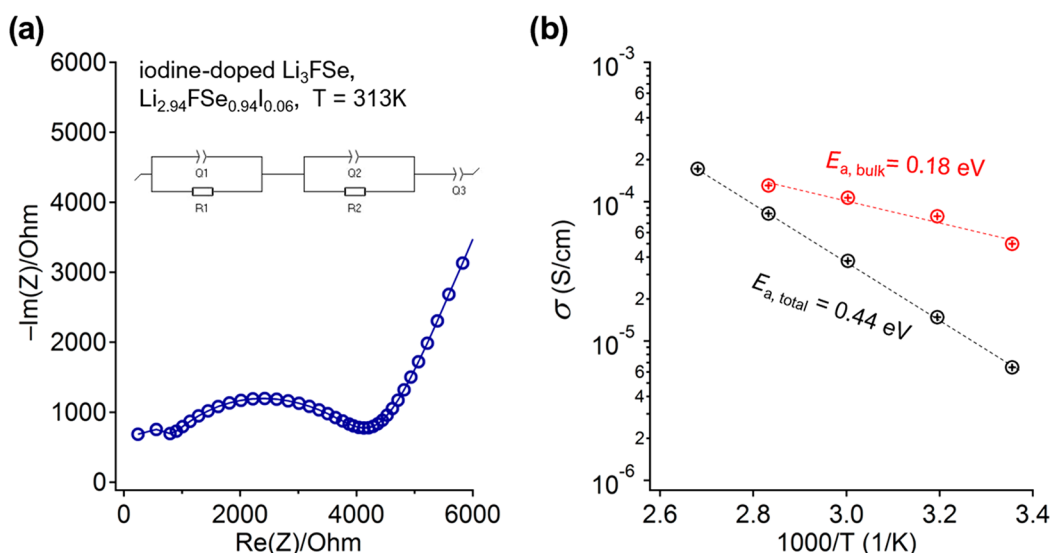


**Figure 8.** (a) Representative Nyquist plot of the cold-pressed iodine-doped  $\text{Li}_3\text{FSe}$  with the refined composition of  $\text{Li}_{2.94}\text{FSe}_{0.94}\text{I}_{0.06}$  showing typical two semicircles in the high- and medium-frequency range and one spike in the low-frequency range. (b) Temperature-dependent total (black circles) and bulk (red circles) ionic conductivity with the extracted activation energy for ionic motion.

migration barrier via the vacancy mechanism in the  $\text{Li}_3\text{FSe}$  grain. Although small amounts of  $\text{LiI}$  impurity were detected in the refinement before, the bulk activation energy of the iodine-doped  $\text{Li}_3\text{FSe}$  antiperovskite is far smaller than that of pure and doped  $\text{LiI}$  ( $E_a \approx 0.4\text{ eV}$ ),<sup>56–58</sup> which suggests that the bulk impedance response only comes from the antiperovskite phase.

The ionic conductivity of the Li-deficient fluorine antiperovskite is also comparable to that of  $\text{Li}_3\text{HCh}$  antiperovskites, for instance, the iodine-doped  $\text{Li}_3\text{HS}$  with total ionic conductivity of  $7.88 \times 10^{-6}\text{ S/cm}$  at room temperature.<sup>21</sup> A comparison with the antiperovskite “ $\text{Li}_3\text{OX}$ ” ( $X = \text{Cl}, \text{Br}$ ) would be helpful, but subsequent studies of the Li conductivity in crystalline “ $\text{Li}_3\text{OX}$ ” compounds have reported the room-temperature conductivities from  $5 \times 10^{-7}$  to  $5 \times 10^{-4}\text{ S/cm}$ ,<sup>18,59,60</sup> with concerns that the as-prepared “ $\text{Li}_3\text{OX}$ ” might be  $\text{Li}_2\text{OHX}$  antiperovskite rather than  $\text{Li}_3\text{OX}$ . Another established fluorine-doped antiperovskite Li-ion conductor,  $\text{Li}_2\text{OHX}$ , was reported for high-voltage all-solid-state Li-ion batteries, and  $\text{Li}_2(\text{OH})_{0.9}\text{F}_{0.1}\text{Cl}$  has shown a measured  $\text{Li}^+$  conductivity of  $3.5 \times 10^{-5}\text{ S/cm}$  and activation energy of  $0.52\text{ eV}$ .<sup>19</sup> The room-temperature ionic conductivity demonstrated in the iodine-doped  $\text{Li}_3\text{FSe}$  antiperovskite is a little lower than those of superionic garnets and LISICON-structured oxide electrolytes.<sup>52,61</sup> Furthermore, the ionic conductivity of the orthorhombic  $\text{Na}_3\text{FS}$  has increased by 3 orders of magnitude when a small amount of sodium vacancies is introduced by halide ( $\text{Br}^-$  and  $\text{I}^-$ ) doping. Likewise, the extracted bulk activation energy of Br-doped  $\text{Na}_3\text{FS}$  agrees well with the calculated migration barrier (Figure S16). Our preliminary optimization by facile halide substitution has enhanced the performance of fluoride-based APs and demonstrated the potential as solid-state electrolytes.

#### 4. CONCLUSION

We have reported the high-pressure synthesis of  $\text{M}_3\text{FCh}$  ( $M = \text{Li}, \text{Na}; \text{Ch} = \text{S}, \text{Se}, \text{Te}$ ) antiperovskites that adopt ideal cubic antiperovskite structures, except for orthorhombic  $\text{Na}_3\text{FS}$ , exhibiting robustness against octahedral distortion, the same as observed in  $\text{M}_3\text{HCh}$  analogues. The first-principles calculation

on these new fluoride-based APs shows that migration barriers for  $\text{Li}^+/\text{Na}^+$  diffusion are as low as the hydride-based ones and reveal the critical role of long-range bonding interactions between chalcogen anions and the moving cations. We unravel the correlation between the octahedral rotation mode, the tolerance factor, and the migration barrier for ionic transport: as the tolerance factor decreases, the rotation mode becomes softer and the migration energy decreases. Our results suggest that cubic APs with the tendency to undergo octahedral distortion are desirable for achieving fast Li/Na ionic diffusion. These findings derived from the lattice dynamics may provide new possibilities for exploring other novel physical properties, such as dielectricity and magnetism.

#### ■ ASSOCIATED CONTENT

##### Supporting Information

The Supporting Information is available free of charge at <https://pubs.acs.org/doi/10.1021/jacs.1c04260>.

Theoretical and experimental details including chemical bonding analysis, X-ray diffraction, and additional data (PDF)

##### Accession Codes

CCDC 2079673–2079676 contain the supplementary crystallographic data for this paper. These data can be obtained free of charge via [www.ccdc.cam.ac.uk/data\\_request/cif](http://www.ccdc.cam.ac.uk/data_request/cif), or by emailing [data\\_request@ccdc.cam.ac.uk](mailto:data_request@ccdc.cam.ac.uk), or by contacting The Cambridge Crystallographic Data Centre, 12 Union Road, Cambridge CB2 1EZ, UK; fax: +44 1223 336033.

#### ■ AUTHOR INFORMATION

##### Corresponding Authors

Akihito Kuwabara – Nanostructures Research Laboratory, Japan Fine Ceramics Center, Nagoya 456-8587, Japan; [orcid.org/0000-0002-2810-3437](https://orcid.org/0000-0002-2810-3437); Email: [kuwabara@jfcc.or.jp](mailto:kuwabara@jfcc.or.jp)

Hiroshi Kageyama – Department of Energy and Hydrocarbon Chemistry, Graduate School of Engineering, Kyoto University, Kyoto 615-8510, Japan; [orcid.org/0000-0002-3911-9864](https://orcid.org/0000-0002-3911-9864); Email: [kage@scl.kyoto-u.ac.jp](mailto:kage@scl.kyoto-u.ac.jp)



## Authors

**Susumu Fujii** – Nanostructures Research Laboratory, Japan Fine Ceramics Center, Nagoya 456-8587, Japan; Division of Materials and Manufacturing Science, Graduate School of Engineering, Osaka University, Osaka 565-0871, Japan

**Shenghan Gao** – Department of Energy and Hydrocarbon Chemistry, Graduate School of Engineering, Kyoto University, Kyoto 615-8510, Japan

**Cédric Tassel** – Department of Energy and Hydrocarbon Chemistry, Graduate School of Engineering, Kyoto University, Kyoto 615-8510, Japan

**Tong Zhu** – Department of Energy and Hydrocarbon Chemistry, Graduate School of Engineering, Kyoto University, Kyoto 615-8510, Japan; [orcid.org/0000-0003-0288-0462](https://orcid.org/0000-0003-0288-0462)

**Thibault Broux** – Department of Energy and Hydrocarbon Chemistry, Graduate School of Engineering, Kyoto University, Kyoto 615-8510, Japan; [orcid.org/0000-0002-4196-9921](https://orcid.org/0000-0002-4196-9921)

**Koji Okada** – Department of Energy and Hydrocarbon Chemistry, Graduate School of Engineering, Kyoto University, Kyoto 615-8510, Japan

**Yuto Miyahara** – Department of Energy and Hydrocarbon Chemistry, Graduate School of Engineering, Kyoto University, Kyoto 615-8510, Japan; [orcid.org/0000-0003-4662-0996](https://orcid.org/0000-0003-4662-0996)

Complete contact information is available at:  
<https://pubs.acs.org/10.1021/jacs.1c04260>

## Author Contributions

#S.F. and S.H.G. contributed equally.

## Notes

The authors declare no competing financial interest.

## ACKNOWLEDGMENTS

This work was supported by a Grant-in-Aid for Scientific Research on Innovative Areas “Mixed Anion” (JP16H06438, JP16H06439, JP16H06440) and JSPS Core-to-Core Program (A) Advanced Research Networks (JPJSCCA20200004).

## REFERENCES

- (1) Peña, M. A.; Fierro, J. L. G. Chemical Structures and Performance of Perovskite Oxides. *Chem. Rev.* **2001**, *101* (7), 1981–2017.
- (2) Acosta, M.; Novak, N.; Rojas, V.; Patel, S.; Vaish, R.; Koruza, J.; Rossetti, G. A.; Rödel, J. BaTiO<sub>3</sub>-Based Piezoelectrics: Fundamentals, Current Status, and Perspectives. *Appl. Phys. Rev.* **2017**, *4* (4), 041305.
- (3) Noheda, B.; Cox, D. E.; Shirane, G.; Gonzalo, J. A.; Cross, L. E.; Park, S. E. A Monoclinic Ferroelectric Phase in the Pb(Zr<sub>1-x</sub>Ti<sub>x</sub>)O<sub>3</sub> Solid Solution. *Appl. Phys. Lett.* **1999**, *74* (14), 2059–2061.
- (4) Suárez, D. Y.; Reaney, I. M.; Lee, W. E. Relation between Tolerance Factor and T<sub>c</sub> in Aurivillius Compounds. *J. Mater. Res.* **2001**, *16* (11), 3139–3149.
- (5) Kawamoto, T.; Fujita, K.; Yamada, I.; Matoba, T.; Kim, S. J.; Gao, P.; Pan, X.; Findlay, S. D.; Tassel, C.; Kageyama, H.; Studer, A. J.; Hester, J.; Irifune, T.; Akamatsu, H.; Tanaka, K. Room-Temperature Polar Ferromagnet ScFeO<sub>3</sub> Transformed from a High-Pressure Orthorhombic Perovskite Phase. *J. Am. Chem. Soc.* **2014**, *136* (43), 15291–15299.
- (6) Li, R. W.; Wang, H.; Wang, X.; Yu, X. Z.; Matsui, Y.; Cheng, Z. H.; Shen, B. G.; Plummer, E. W.; Zhang, J. Anomalous Large Anisotropic Magnetoresistance in a Perovskite Manganite. *Proc. Natl. Acad. Sci. U. S. A.* **2009**, *106* (34), 14224–14229.
- (7) Torrance, J. B.; Lacorre, P.; Nazzari, A. I.; Ansaldo, E. J.; Niedermayer, C. Systematic Study of Insulator-Metal Transitions in Perovskites RNiO<sub>3</sub> (R = Pr, Nd, Sm, Eu) Due to Closing of Charge-Transfer Gap. *Phys. Rev. B: Condens. Matter Mater. Phys.* **1992**, *45* (14), 8209–8212.
- (8) Li, X.; Benedek, N. A. Enhancement of Ionic Transport in Complex Oxides through Soft Lattice Modes and Epitaxial Strain. *Chem. Mater.* **2015**, *27* (7), 2647–2652.
- (9) Cava, R. J.; Batlogg, B.; Krajewski, J. J.; Farrow, R.; Rupp, L. W.; White, A. E.; Short, K.; Peck, W. F.; Kometani, T. Superconductivity near 30 K without Copper: The Ba<sub>0.6</sub>K<sub>0.4</sub>BiO<sub>3</sub> Perovskite. *Nature* **1988**, *332*, 814–816.
- (10) Pei, S.; Jorgensen, J. D.; Dabrowski, B.; Hinks, D. G.; Richards, D. R.; Mitchell, A. W.; Newsam, J. M.; Sinha, S. K.; Vaknin, D.; Jacobson, A. J. Structural Phase Diagram of the Ba<sub>1-x</sub>K<sub>x</sub>BiO<sub>3</sub> System. *Phys. Rev. B: Condens. Matter Mater. Phys.* **1990**, *41* (7), 4126–4141.
- (11) Wang, Y.; Zhang, H.; Zhu, J.; Lü, X.; Li, S.; Zou, R.; Zhao, Y. Antiperovskites with Exceptional Functionalities. *Adv. Mater.* **2020**, *32* (7), 1905007.
- (12) Kageyama, H.; Hayashi, K.; Maeda, K.; Attfield, J. P.; Hiroi, Z.; Rondinelli, J. M.; Poeppelmeier, K. R. Expanding Frontiers in Materials Chemistry and Physics with Multiple Anions. *Nat. Commun.* **2018**, *9* (1), 772.
- (13) Oudah, M.; Ikeda, A.; Hausmann, J. N.; Yonezawa, S.; Fukumoto, T.; Kobayashi, S.; Sato, M.; Maeno, Y. Superconductivity in the Antiperovskite Dirac-Metal Oxide Sr<sub>3-x</sub>SnO. *Nat. Commun.* **2016**, *7*, 13617.
- (14) Takahashi, T.; Yamamoto, O. The Ag/Ag<sub>3</sub>SI/I<sub>2</sub> Solid-Electrolyte Cell. *Electrochim. Acta* **1966**, *11* (7), 779–789.
- (15) Kamishima, K.; Goto, T.; Nakagawa, H.; Miura, N.; Ohashi, M.; Mori, N.; Sasaki, T.; Kanomata, T. Giant Magnetoresistance in the Intermetallic Compound Mn<sub>3</sub>GaC. *Phys. Rev. B: Condens. Matter Mater. Phys.* **2000**, *63* (2), 024426.
- (16) Song, X.; Sun, Z.; Huang, Q.; Rettenmayr, M.; Liu, X.; Seyring, M.; Li, G.; Rao, G.; Yin, F. Adjustable Zero Thermal Expansion in Antiperovskite Manganese Nitride. *Adv. Mater.* **2011**, *23* (40), 4690–4694.
- (17) He, T.; Huang, Q.; Ramirez, A. P.; Wang, Y.; Regan, K. A.; Rogado, N.; Hayward, M. A.; Haas, M. K.; Slusky, J. S.; Inumara, K.; Zandbergen, H. W.; Ong, N. P.; Cava, R. J. Superconductivity in the Non-Oxide Perovskite MgCNi<sub>3</sub>. *Nature* **2001**, *411* (6833), 54–56.
- (18) Zhao, Y.; Daemen, L. L. Superionic Conductivity in Lithium-Rich Anti-Perovskites. *J. Am. Chem. Soc.* **2012**, *134* (36), 15042–15047.
- (19) Li, Y.; Zhou, W.; Xin, S.; Li, S.; Zhu, J.; Xujie, L.; Cui, Z.; Jia, Q.; Zhou, J.; Zhao, Y.; Goodenough, J. B. Fluorine-Doped Antiperovskite Electrolyte for All-Solid-State Lithium-Ion Batteries. *Angew. Chem., Int. Ed.* **2016**, *55* (34), 9965–9968.
- (20) Sun, Y.; Wang, Y.; Liang, X.; Xia, Y.; Peng, L.; Jia, H.; Li, H.; Bai, L.; Feng, J.; Jiang, H.; Xie, J. Rotational Cluster Anion Enabling Superionic Conductivity in Sodium-Rich Antiperovskite Na<sub>3</sub>OBH<sub>4</sub>. *J. Am. Chem. Soc.* **2019**, *141* (14), 5640–5644.
- (21) Gao, S.; Broux, T.; Fujii, S.; Tassel, C.; Yamamoto, K.; Xiao, Y.; Oikawa, I.; Takamura, H.; Ubukata, H.; Watanabe, Y.; Fujii, K.; Yashima, M.; Kuwabara, A.; Uchimoto, Y.; Kageyama, H. Hydride-Based Antiperovskites with Soft Anionic Sublattices as Fast Alkali Ionic Conductors. *Nat. Commun.* **2021**, *12*, 201.
- (22) Kamaya, N.; Homma, K.; Yamakawa, Y.; Hirayama, M.; Kanno, R.; Yonemura, M.; Kamiyama, T.; Kato, Y.; Hama, S.; Kawamoto, K.; Mitsui, A. A Lithium Superionic Conductor. *Nat. Mater.* **2011**, *10* (9), 682–686.
- (23) Deiseroth, H. J.; Kong, S. T.; Eckert, H.; Vannahme, J.; Reiner, C.; Zaiß, T.; Schlosser, M. Li<sub>6</sub>PS<sub>3</sub>X: A Class of Crystalline Li-Rich Solids with an Unusually High Li<sup>+</sup> Mobility. *Angew. Chem., Int. Ed.* **2008**, *47* (4), 755–758.
- (24) Wang, Y.; Richards, W. D.; Ong, S. P.; Miara, L. J.; Kim, J. C.; Mo, Y.; Ceder, G. Design Principles for Solid-State Lithium Superionic Conductors. *Nat. Mater.* **2015**, *14* (10), 1026–1031.

- (25) Yamashita, H.; Broux, T.; Kobayashi, Y.; Takeiri, F.; Ubukata, H.; Zhu, T.; Hayward, M. A.; Fujii, K.; Yashima, M.; Shitara, K.; Kuwabara, A.; Murakami, T.; Kageyama, H. Chemical Pressure-Induced Anion Order-Disorder Transition in LnHO Enabled by Hydride Size Flexibility. *J. Am. Chem. Soc.* **2018**, *140* (36), 11170–11173.
- (26) Broux, T.; Ubukata, H.; Pickard, C. J.; Takeiri, F.; Kobayashi, G.; Kawaguchi, S.; Yonemura, M.; Goto, Y.; Tassel, C.; Kageyama, H. High-Pressure Polymorphs of LaHO with Anion Coordination Reversal. *J. Am. Chem. Soc.* **2019**, *141* (22), 8717–8720.
- (27) Yamamoto, T.; Zeng, D.; Kawakami, T.; Arcisauskaitė, V.; Yata, K.; Patino, M. A.; Izumo, N.; McGrady, J. E.; Kageyama, H.; Hayward, M. A. The Role of  $\pi$ -Blocking Hydride Ligands in a Pressure-Induced Insulator-to-Metal Phase Transition in SrVO<sub>2</sub>H. *Nat. Commun.* **2017**, *8* (1), 1217.
- (28) Blöchl, P. E. Projector Augmented-Wave Method. *Phys. Rev. B: Condens. Matter Mater. Phys.* **1994**, *50* (24), 17953–17979.
- (29) Perdew, J. P.; Ruzsinszky, A.; Csonka, G. I.; Vydrov, O. A.; Scuseria, G. E.; Constantin, L. A.; Zhou, X.; Burke, K. Restoring the Density-Gradient Expansion for Exchange in Solids and Surfaces. *Phys. Rev. Lett.* **2008**, *100* (13), 136406.
- (30) Kresse, G.; Hafner, J. Ab Initio Molecular-Dynamics Simulation of the Liquid-Metal–Amorphous-Semiconductor Transition in Germanium. *Phys. Rev. B: Condens. Matter Mater. Phys.* **1994**, *49* (20), 14251–14269.
- (31) Kresse, G.; Furthmüller, J. Efficient Iterative Schemes for Ab Initio Total-Energy Calculations Using a Plane-Wave Basis Set. *Phys. Rev. B: Condens. Matter Mater. Phys.* **1996**, *54* (16), 11169–11186.
- (32) Parlinski, K.; Li, Z.; Kawazoe, Y. First-Principles Determination of the Soft Mode in Cubic ZrO<sub>2</sub>. *Phys. Rev. Lett.* **1997**, *78* (21), 4063–4066.
- (33) Togo, A.; Tanaka, I. First Principles Phonon Calculations in Materials Science. *Sr. Mater.* **2015**, *108*, 1–5.
- (34) Pick, R. M.; Cohen, M. H.; Martin, R. M. Microscopic Theory of Force Constants in the Adiabatic Approximation. *Phys. Rev. B* **1970**, *1* (2), 910–920.
- (35) Mills, G.; Jónsson, H.; Schenter, G. K. Reversible Work Transition State Theory: Application to Dissociative Adsorption of Hydrogen. *Surf. Sci.* **1995**, *324* (2–3), 305–337.
- (36) Henkelman, G.; Uberuaga, B. P.; Jónsson, H. Climbing Image Nudged Elastic Band Method for Finding Saddle Points and Minimum Energy Paths. *J. Chem. Phys.* **2000**, *113* (22), 9901–9904.
- (37) Goldschmidt, V. M. Die Gesetze Der Kristallochemie. *Naturwissenschaften* **1926**, *14* (21), 477–485.
- (38) Shannon, R. D. Revised Effective Ionic Radii and Systematic Studies of Interatomic Distances in Halides and Chalcogenides. *Acta Crystallogr., Sect. A: Cryst. Phys., Diff., Theor. Gen. Crystallogr.* **1976**, *32* (5), 751–767.
- (39) Kim, K.; Siegel, D. J. Correlating Lattice Distortions, Ion Migration Barriers, and Stability in Solid Electrolytes. *J. Mater. Chem. A* **2019**, *7* (7), 3216–3227.
- (40) Wu, F.; Lee, J. T.; Xiao, Y.; Yushin, G. Nanostructured Li<sub>2</sub>Se Cathodes for High Performance Lithium-Selenium Batteries. *Nano Energy* **2016**, *27*, 238–246.
- (41) Oishi, R.; Yonemura, M.; Nishimaki, Y.; Torii, S.; Hoshikawa, A.; Ishigaki, T.; Morishima, T.; Mori, K.; Kamiyama, T. Rietveld Analysis Software for J-PARC. *Nucl. Instrum. Methods Phys. Res., Sect. A* **2009**, *600* (1), 94–96.
- (42) Momma, K.; Izumi, F. VESTA 3 for Three-Dimensional Visualization of Crystal, Volumetric and Morphology Data. *J. Appl. Crystallogr.* **2011**, *44* (6), 1272–1276.
- (43) Gale, J. D. GULP: A Computer Program for the Symmetry-Adapted Simulation of Solids. *J. Chem. Soc., Faraday Trans.* **1997**, *93* (4), 629–637.
- (44) Tadano, T.; Tsuneyuki, S. Self-Consistent Phonon Calculations of Lattice Dynamical Properties in Cubic SrTiO<sub>3</sub> with First-Principles Anharmonic Force Constants. *Phys. Rev. B: Condens. Matter Mater. Phys.* **2015**, *92* (5), 054301.
- (45) Rodríguez-Carvajal, J.; Hennion, M.; Moussa, F.; Moudden, A.; Pinsard, L.; Revcolevschi, A. Neutron-Diffraction Study of the Jahn-Teller Transition in Stoichiometric. *Phys. Rev. B: Condens. Matter Mater. Phys.* **1998**, *57* (6), R3189–R3192.
- (46) Brese, N. E.; O'Keeffe, M. Bond-valence Parameters for Solids. *Acta Crystallogr., Sect. B: Struct. Sci.* **1991**, *47* (2), 192–197.
- (47) Nelson, R.; Ertural, C.; George, J.; Deringer, V. L.; Hautier, G.; Dronskowski, R. LOBSTER: Local Orbital Projections, Atomic Charges, and Chemical-Bonding Analysis from Projector-Augmented-Wave-Based Density-Functional Theory. *J. Comput. Chem.* **2020**, *41* (21), 1931–1940.
- (48) Dronskowski, R.; Blöchl, P. E. Crystal Orbital Hamilton Populations (COHP). Energy-Resolved Visualization of Chemical Bonding in Solids Based on Density-Functional Calculations. *J. Phys. Chem.* **1993**, *97* (33), 8617–8624.
- (49) Deringer, V. L.; Tchougréeff, A. L.; Dronskowski, R. Crystal Orbital Hamilton Population (COHP) Analysis as Projected from Plane-Wave Basis Sets. *J. Phys. Chem. A* **2011**, *115* (21), 5461–5466.
- (50) Muy, S.; Bachman, J. C.; Giordano, L.; Chang, H. H.; Abernathy, D. L.; Bansal, D.; Delaire, O.; Hori, S.; Kanno, R.; Maglia, F.; Lupart, S.; Lamp, P.; Shao-Horn, Y. Tuning Mobility and Stability of Lithium Ion Conductors Based on Lattice Dynamics. *Energy Environ. Sci.* **2018**, *11* (4), 850–859.
- (51) Krauskopf, T.; Muy, S.; Culver, S. P.; Ohno, S.; Delaire, O.; Shao-Horn, Y.; Zeier, W. G. Comparing the Descriptors for Investigating the Influence of Lattice Dynamics on Ionic Transport Using the Superionic Conductor Na<sub>3</sub>PS<sub>4-x</sub>Se<sub>x</sub>. *J. Am. Chem. Soc.* **2018**, *140* (43), 14464–14473.
- (52) Bachman, J. C.; Muy, S.; Grimaud, A.; Chang, H. H.; Pour, N.; Lux, S. F.; Paschos, O.; Maglia, F.; Lupart, S.; Lamp, P.; Giordano, L.; Shao-Horn, Y. Inorganic Solid-State Electrolytes for Lithium Batteries: Mechanisms and Properties Governing Ion Conduction. *Chem. Rev.* **2016**, *116* (1), 140–162.
- (53) Kraft, M. A.; Culver, S. P.; Calderon, M.; Böcher, F.; Krauskopf, T.; Senyshyn, A.; Dietrich, C.; Zevalkink, A.; Janek, J.; Zeier, W. G. Influence of Lattice Polarizability on the Ionic Conductivity in the Lithium Superionic Argyrodites Li<sub>6</sub>PS<sub>5</sub>X (X = Cl, Br, I). *J. Am. Chem. Soc.* **2017**, *139* (31), 10909–10918.
- (54) Liang, J.; Li, X.; Wang, S.; Adair, K. R.; Li, W.; Zhao, Y.; Wang, C.; Hu, Y.; Zhang, L.; Zhao, S.; Lu, S.; Huang, H.; Li, R.; Mo, Y.; Sun, X. Site-Occupation-Tuned Superionic Li<sub>6</sub>ScCl<sub>3+x</sub> Halide Solid Electrolytes for All-Solid-State Batteries. *J. Am. Chem. Soc.* **2020**, *142* (15), 7012–7022.
- (55) Feng, X.; Chien, P. H.; Zhu, Z.; Chu, I. H.; Wang, P.; Immediato-Scuotto, M.; Arabzadeh, H.; Ong, S. P.; Hu, Y. Y. Studies of Functional Defects for Fast Na-Ion Conduction in Na<sub>3-y</sub>PS<sub>4-x</sub>Cl<sub>x</sub> with a Combined Experimental and Computational Approach. *Adv. Funct. Mater.* **2019**, *29* (9), 1–9.
- (56) Schlaikjer, C. R.; Liang, C. C. Ionic Conduction in Calcium Doped Polycrystalline Lithium Iodide. *J. Electrochem. Soc.* **1971**, *118* (9), 1447.
- (57) Jackson, B. J. H.; Young, D. A. Ionic Conduction in Pure and Doped Single-Crystalline Lithium Iodide. *J. Phys. Chem. Solids* **1969**, *30* (8), 1973–1976.
- (58) Poulsen, F. W. Ionic Conductivity of Solid Lithium Iodide and Its Monohydrate. *Solid State Ionics* **1981**, *2* (1), 53–57.
- (59) Hood, Z. D.; Wang, H.; Samuthira Pandian, A.; Keum, J. K.; Liang, C. Li<sub>2</sub>OHCl Crystalline Electrolyte for Stable Metallic Lithium Anodes. *J. Am. Chem. Soc.* **2016**, *138* (6), 1768–1771.
- (60) Hanghofer, I.; Redhammer, G. J.; Rohde, S.; Hanzu, I.; Senyshyn, A.; Wilkening, H. M. R.; Rettenwander, D. Untangling the Structure and Dynamics of Lithium-Rich Anti-Perovskites Envisaged as Solid Electrolytes for Batteries. *Chem. Mater.* **2018**, *30* (22), 8134–8144.
- (61) Ohno, S.; Banik, A.; Dewald, G. F.; Kraft, M. A.; Krauskopf, T.; Minafra, N.; Till, P.; Weiss, M.; Zeier, W. G. Materials Design of Ionic Conductors for Solid State Batteries. *Prog. Energy* **2020**, *2* (2), 022001.